Microfluidic approach for rapid multicomponent interfacial tensiometry†

João T. Cabral‡ and Steven D. Hudson*

Received 23rd August 2005, Accepted 23rd December 2005
First published as an Advance Article on the web 1st February 2006
DOI: 10.1039/b511976f

We report a microfluidic instrument to rapidly measure the interfacial tension of multicomponent immiscible liquids. The measurement principle rests upon the deformation and retraction dynamics of drops under extensional flow and was implemented for the first time in microfluidics (S. D. Hudson *et al.*, *Appl. Phys. Lett.,* 2005, **87**, 081905 (ref. 1)). Here we describe in detail the instrument design and physics and extend this principle to investigate multicomponent mixtures, specifically two-component drops of adjustable composition. This approach provides fast real-time σ measurements (on the order of 1 s), the possibility of rapidly adjusting drop composition and utilizes small sample volumes (approximately 10 μL). The tensiometer operation is illustrated with water drops and binary drops (water/ethylene glycol mixtures) in silicone oils. The technique should be particularly valuable for high-throughput characterization of complex fluids.

I. Introduction

Multiphase liquid systems, like foams and emulsions, are ubiquitous in nature and find countless everyday applications, including foods, pharmaceutics, cosmetics, paints, agrochemicals and oil recovery. The morphology and (meta-)stability of these often complex immiscible mixtures is largely controlled by their interfacial tension (IFT, σ) and related dynamic properties. Accurate and rapid IFT measurements are, therefore, both practically and scientifically important. In thermodynamic terms, IFT is the Helmoltz Free energy change with surface area and a measure of the excess cohesive energy of a liquid interface. Experimental measurements rest on the mechanical definition of IFT: the differential reversible work (W) required to stretch an interface, normalized to that interfacial area (A), $\sigma = (\partial W/\partial A)$, which corresponds to the magnitude of the force acting parallel to that interface per unit edge length (equivalent units are, therefore, 1 erg cm^{-2} = 1 mJ m^{-2} = 1 mN m^{-1}).

Surface and interfacial tension research has spanned over two centuries, since the pioneering work of Young, Laplace and Gauss in the early 19th century. Classical and modern IFT measurement techniques have been reviewed in detail by several authors.[2–4] Measurement methods are customarily divided into static and dynamic. The former involves the determination of the (axisymmetric) shape of bubbles/drops or the profile of menisci under a given force equilibrium. Common techniques include sessile drop and pendant drop methods, in which the interfacial tension is determined by the distortion of drop shape by gravity, which elongates or flattens otherwise spherical drops. Earlier surface tension measurements, also resting on the balance between capillarity and gravitational forces, include the capillary rise and drop volume (or weight) methods, which consist in measuring the height of a meniscus in a partially immersed capillary, or the volume (or weight) of drops falling from a capillary. Measurements of the capillary and hydrostatic pressures of drops and bubbles forced out of a capillary can also yield IFT (*e.g.*, maximum bubble pressure method). Alternatively, IFT can be obtained directly using a microbalance and measuring the force acting on a probe which is static and/or detaching off a liquid interface. Probes include a thin plate (Wilhelmy method), ring (Du Noüy method), sphere, cone, cylinder, *etc.* Extremely low interfacial tensions can be measured by the spinning drop (and spinning rod) method, from the balance of centrifugal and interfacial forces in a rapidly rotating field. This method also uses profile analysis of deformed drops (into cylinders or long ellipsoids), and can reach IFTs down to 10^{-6} mN m^{-1}, depending on the density differences and drop volume.

Dynamic interfacial tensiometry is necessary to study immiscible fluid mixtures that contain surface active components or solutes (*e.g.* surfactants, salts, particles). Newly created interfaces are hence generally out of equilibrium and require time for compositional redistribution (including adsorption) to occur. Dynamic measurements[4,5] probe such time evolution of the IFT as an interface ages toward equilibrium. Most of the techniques enumerated above can monitor IFT changes in time, within certain observation windows (reviewed in ref. 5). Additional approaches capable of studying fresh interfaces include the oscillating jet and capillary wave methods.[2]

All aforementioned IFT techniques offer advantages and shortcomings[4] relating to the range of accessible IFTs and measurable interface ages, the necessary equilibration time prior to experiments, the amount of sample required, or the susceptibility to impurities and surface wetting. Measurements with varying drop or matrix composition are generally carried

Polymers Division, National Institute of Standards and Technology, Gaithersburg, MD 20899 E-mail: Steven.Hudson@nist.gov
† Electronic supplementary information (ESI) available: Fig. S1 and S2. See DOI: 10.1039/b511976f
‡ Present address: Department of Chemical Engineering, Imperial College London, London SW7 2AZ, UK. E-mail: Joao.Cabral@imperial.ac.uk.

out in series and become rather time-consuming due to the setup of experiments. Only recently, the pendant drop (and growing drop[6]) tensiometry approach has been modified to permit composition changes of the matrix fluid where the drop is immersed and to facilitate the study of sorption/desorption dynamics.[7]

The tremendous progress of microfluidics during the past two decades, in particular the demonstration of the production of well controlled droplet dispersions[8–12] and the manipulation of tailored confined flow fields,[13] lead us to seek to design, fabricate, and implement a microfluidic tensiometer. Such an instrument should be able to produce drops and interrogate them under flow, while their shape is continuously recorded using optical microscopy. The advent of topographic microfluidic mixers, in both miscible flows (which are otherwise laminar)[14–16] and immiscible plug flows,[17,18] suggests that both the composition of the drops and matrix fluid can be varied and adjusted during an experiment. Additionally, the correspondence of time and position of drop formation and flow along microchannels[17,18] indicates opportunities for the study of interfacial dynamics. Finally, we are motivated by the inherent advantages of microfluidics, including the handling of small sample volumes, which reduces reagent cost and waste, device miniaturization and portability, unique flow control, and usually an enhanced throughput.[19]

This paper is organized as follows: section II provides the theoretical background of drop shape dynamics under extensional flow utilized in this approach. The design and fabrication of the microfluidic device is described in section III. The tensiometer operation, including flow control, data acquisition, analysis and interpretation is detailed in section IV. We demonstrate the operation of the microfluidic tensiometer with model oil/water binary and ternary systems, and discuss factors affecting the applicability of the theoretical analysis and the precision and accuracy of measurements in section V. Section VI summarizes the findings and provides an outlook of future work.

II. Theoretical background

The dynamics of deformation and retraction of an isolated drop subject to an unbounded extensional flow field are well established.[20,21] In short, a spheroidal drop of a Newtonian fluid deforms according to

$$\frac{\partial D}{\partial t^*} = D_{\text{steady}} - D = \frac{5}{2\hat{\eta}+3}\tau\dot{\varepsilon} - D \tag{1}$$

where D is the scalar drop deformation parameter defined by the difference of major and minor radii of the spheroid, respectively a and b, divided by their sum,

$$D = \frac{a-b}{a+b} \tag{2}$$

t^* is dimensionless time ($t^* \equiv t/\tau$) and $\dot{\varepsilon}$ is the surrounding fluid extension rate. The characteristic time τ for drop shape relaxation depends on the drop equilibrium radius a_0, the viscosities of the fluids and interfacial tension σ, as

$$\tau = \frac{\alpha\eta_c a_0}{\sigma} \tag{3}$$

where $\alpha\eta_c$ is an 'effective' (or equivalent) viscosity, with

$$\alpha = \left[\frac{(2\hat{\eta}+3)(19\hat{\eta}+16)}{40(\hat{\eta}+1)}\right] \tag{4}$$

and $\hat{\eta} = \eta_d/\eta_c$ is the relative viscosity between the drop (η_d) and matrix (η_c). In quiescent conditions (absence of flow) or at uniform flow velocity, drop shape relaxation toward equilibrium is exponential in time as eqn (1) becomes simply

$$D(t) = D_0\exp(-t/\tau) \tag{5}$$

where D_0 is the deformation at the instant $t = 0$. In extensional flow (under an accelerating or decelerating flow field), drop deformation D generally depends both on the steady-state deformation, determined by the extension rate $\dot{\varepsilon}$, and on drop shape history. The first term of eqn (1) often dominates drop dynamics and, in a 'quasi-steady-state approximation', the instantaneous deformation becomes essentially $D \approx D_{\text{steady}}$, as the drop response to a new extension rate is immediate ($dD/dt^* \approx 0$). However, for rapidly accelerating flows, the material rate of change of the extension rate ($d\dot{\varepsilon}\tau^2/dt$) becomes non-negligible, and the instantaneous deformation of the drop lags its steady state deformation. In that general case, eqn (1) must be considered in full. For unidirectional time-invariant extensional flow (along x), with extension rate, $\dot{\varepsilon} = du/dx$, we express the material time derivative of D as $\frac{dD}{dt} \equiv u\frac{\partial D}{\partial x}$, and rewrite eqn (1) in a convenient form:

$$\alpha\eta_c\left(\frac{5}{2\hat{\eta}+3}\dot{\varepsilon} - u\frac{\partial D}{\partial x}\right) = \sigma\left(\frac{D}{a_0}\right) \tag{6}$$

.

A graphic representation of eqn (6) against D/a_0 yields a straight line of slope σ, the interfacial tension between the two liquids. This relation generally applies to modest deformations of spheroidal drops of Newtonian fluids, typically for $D < 0.15$,[20,21] and to uniaxial and planar elongational flows. In the latter case, the drop remains essentially spheroidal, because equilibration of the minor axes is a faster mode of relaxation than retraction of a spheroid.[22]

With these ideas in mind, we develop a rapid interfacial tensiometer based on time-dependent measurements of drop shape undergoing small deformation in extensional flows. Microfluidics emerges as an ideal environment to implement such measurements since (i) fluid droplets of prescribed dimensions can be readily produced[8–11,17,18] and (ii) a plethora of confined flow fields can be generated *via* microchannel geometry and tailoring of relative flow rates.[13,10]

III. Microfluidic device

IIIa. Design

This microfluidic approach to measure IFT interrogates the response of isolated drops in a carrier fluid to extensional flow and thereby obtains the interfacial tension between the fluids. A microfluidic tensiometer device should therefore (i) produce fluid drops and (ii) induce drop deformation and retraction. It must include at least two inputs, for the two immiscible fluids, and one output. In order to enable the study of mixtures, our

design includes two inputs (for two miscible fluids) and one input for an immiscible stream that encapsulates them into isolated, suspended drops. We label them inputs (1a), (1b) for the miscible liquids and (2) for the immiscible matrix, or continuous, fluid, according to Fig. 1a. While drops of controlled size can be produced at T-junctions[8] (or focusing junctions[9,11]) at capillary number $Ca \approx 1$ ($Ca = \eta_c u/\sigma$, where u is the flow velocity), we chose to produce fluid plugs at lower Ca ($\approx 10^{-4}$). This allows the systematic production of drops of uniform size under confinement, almost independently of σ, which is advantageous when investigating mixtures of varied composition. Moreover, the shear forces that could induce unwanted compositional heterogeneity of drops (*e.g.*, sweeping of surfactant to the deforming interface) are kept to a minimum. Drop size then becomes comparable to the dimensions of the channels in which they are produced. The T-junction therefore intercalates plugs of liquids (1a + 1b) between plugs of liquid (2), as illustrated in Fig. 2a with drops of water and ethylene glycol in an oil matrix.

Our approach rests on probing the response of suspended drops in a fluid so we convert the fluid plugs into drops by flowing into a relatively spacious channel (4), where measurements take place and where hydrodynamic interactions with the walls do not induce extra drop deformation nor slow their relaxation. To prevent the collision of subsequent plugs as they slow down in a channel of larger cross-section, two additional symmetric streams (3a and 3b) are introduced to accelerate the newly formed drops. The geometry of this 'flow focusing' junction was designed with the assistance of flow simulation (ESI Fig. S1†), so as to maintain the drops' original velocity constant. Fig. 2a depicts the geometry of the focusing junction across the plug-to-drop transition. When channels 3a and b enter at an angle, as shown in Fig. 2a, the drop velocity transitions smoothly, as desired. Notably, a junction with diametrically opposing jets does not accomplish this objective, as the resulting flow field has a steep spatial gradient that would either allow drop coalescence or pulverize the drops, depending on flow rate.

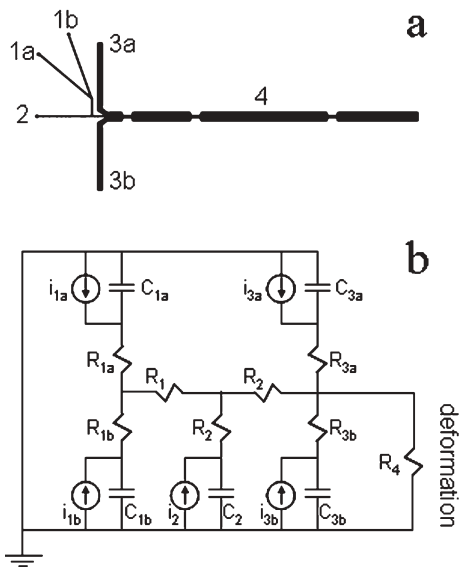

Fig. 1 Microfluidic tensiometer design and corresponding electric circuit analog. Each syringe pump is depicted by a current source and capacitor in parallel. The latter mediates changes in the commanded flow rate until the syringe pressure has stabilized. Microchannel dimensions (cross-section and length) are adjusted to stabilize flow, particularly at the plug formation junction, and enhance flow response.

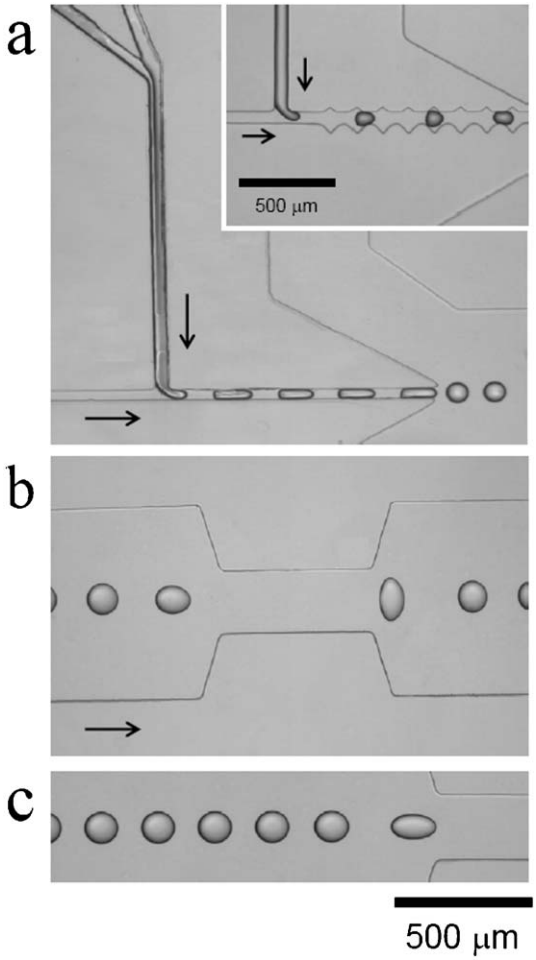

Fig. 2 Optical micrographs depicting the operation of the μIFT device, shown schematically in Fig. 1. (a) Liquid plugs of the two input fluids (1a, 1b, as defined in Fig. 1) are intercalated with the carrier fluid (2) and become drops when entering the wide channel (4) where flow constrictions are distributed along its length. Two additional inputs maintain the drop velocity nearly constant as they transition to the wider channel, and can be used to accelerate drops and increase their spacing. Inset: A drop formation junction followed by a ridged microchannel that induces internal circulation in the drop and therefore promotes mixing of its components. (b) Drops elongate along the direction of flow before the flow constriction and orthogonal to it thereafter. (c) Sequence of drops deforming progressively in an extensional flow gradient caused by a flow constriction. Although the drops with the most severe deformation have complex shapes, the spheroidal description is accurate for those with D less than approximately 0.1. All micrographs are freeze-frame images depicting several drops. In this demonstration, the drop phase is a water/ethylene glycol mixture and the continuous phase is PPMS oil. Arrows indicate the direction of flow.

Drop deformation occurs in an extensional gradient flow field generated by a microchannel constriction. We seek to

induce modest deformations, to which the Taylor theory applies ($D < 0.15$), and have typically chosen a 3:1 contraction of channel width over a length comparable to the width. A constriction induces extension along the flow direction near the entrance, and orthogonal to it upon exit, as illustrated in Fig. 2b. Three of such constrictions were incorporated in the design shown here.

Having specified the necessary components of the microfluidic tensiometer, we next enumerate performance criteria for the device and optimize the design to meet them. An electric circuit analog, shown in Fig. 1b, assists the device design. Each fluid input corresponds to a syringe pump, which is represented by a current source (i) and capacitor (C) in parallel. The latter mediates changes in the commanded flow rate until the syringe pressure has stabilized and results from the compressibility of fluids (exacerbated for gases) and mechanical compliance of the system (tubing, syringe plunger, and fittings). Each microchannel offers a certain resistance to flow, $R \approx 12\eta L/(w_x w_y^3)$, where L is the length of a channel and w_y is the smaller of the two dimensions (w_x, w_y) of its rectangular cross-section. In the present case, therefore, w_y corresponds to the channel height.

The most important requisites for efficient performance of the microfluidic tensiometer are (i) flow stability, in particular at the drop formation node (channels 1 and 2), and (ii) a responsive flow control. The former involves stabilizing the pressures around the T-junction and is necessary for controlled production of monodisperse plugs with adequate size and spacing. The latter ensures that the response time to a composition change is minimal and that nominal compositions are accurate.

Generally, the overall resistance should be kept to a minimum to avoid large pressure drops ($\Delta P = RQ$, where Q is flow rate) that could result in failure of the device and connector seals (typically 500 kPa). Particularly, the resistance along the main channel R_4 should be as small as possible, achieved by making it sufficiently wide and relatively short. The circuit's capacitance should also be low, in particular for inputs 1 and 2, which can be accomplished by utilizing stiff capillary tubing (*e.g.*, Teflon, rather than silicone) of rather short length. Air bubbles introduce significant capacitance in the system, because of their compressibility, and must be avoided. This can be achieved by pressurizing the device (*e.g.*, closing the outlet) and forcing the air to diffuse out through the permeable PDMS.

In order to eliminate transient flows and cross talk between channels 1a and 1b, which would lead to inaccurate metering of input miscible fluids and therefore drop composition, as discussed later, R_{1a} and R_{1b} should be large (in fact, larger than any resistance downstream such as R_1 or R_4), to prevent backflows. This is effectively accomplished by designing channels with small cross-section and appreciable length. Although channel 1 should be narrow to promote diffusive mixing (of 1a and 1b), R_1 should be kept significantly smaller than R_{1a} and R_{1b}, to contribute to stability at the (1a, 1b) junction. The resistances downstream of the plug formation T-junction, R_2 and R_4, should be smaller than upstream. Since R_2 has a narrow cross-section at the T by construction, it is designed to be quite short. A short length after drop production is also necessary in order to test fresh interfaces.

IIIb. Fabrication[23]

The microfluidic tensiometer device was fabricated by conventional rapid prototyping methods, following a procedure depicted in Fig. 3. Photomasks were designed using a graphics program (Canvas or Photoshop 7) and printed on an acetate sheet with a commercial 5080 dpi resolution imagesetter (Pageworks, MA). Earlier iterations of the design were printed using a black and white 1200 dpi printer (HP Laserjet 8000N) on regular transparency film (CG3300, 3M). The master was fabricated by contact photolithography using SU8-2025 or 2075 resists (Microchem) spin coated on a plasma-cleaned silicon wafer (4 inch diameter, Wafer World) and dried. Exposure was carried out with a 365 nm (UVA) Spectroline SB-100P flood lamp, equipped with a 100 Watt Mercury lamp (Spectronics), and placed 50 cm from the specimens, for improved collimation. UV exposure lasted for typically 10 min, depending on specimen thickness and light intensity (200–300) μW cm^{-2}, which was measured with a digital radiometer Spectroline DRC-100X and a 365A UV-A sensor (Spectronics). After baking (beginning at 65 °C, heating 1 °C min^{-1}, and holding at 95 °C for 30 min), the master was developed (PM acetate, Microchem), rinsed with isopropanol,

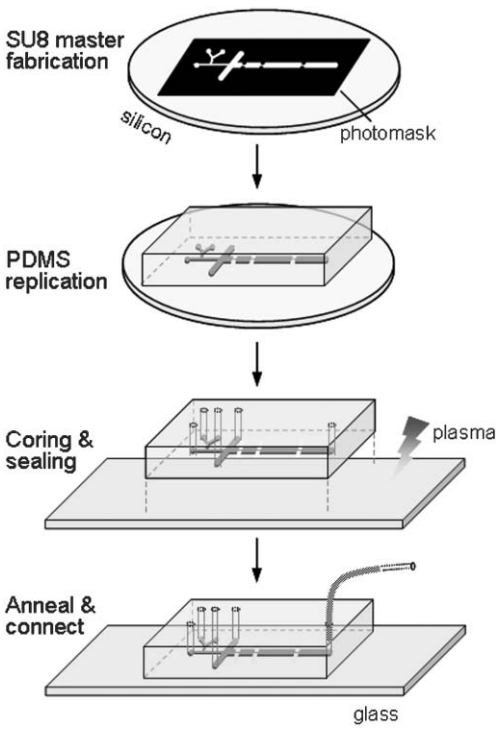

Fig. 3 Schematic of device fabrication and assembly. A microfluidic master is fabricated by contact photolithography using a printed optical mask[30,24] and replicated onto a transparent elastomer (PDMS). The PDMS slab is cored and sealed against a microscope glass slide after oxidation (plasma or UV-ozone) of both surfaces. Finally, the device inputs and output are connected to syringe pumps using flexible tubing.

dried with compressed nitrogen gas and finally baked at 150 °C on a hot plate for approximately 30 min.

A complementary master fabrication technique was also employed to produce 3-dimensional features upon modulated light exposure[24] by photolithography of multifunctional thiolene copolymers (optical adhesive 81, Norland Products).[24,25] This method was used to prepare masters non-planar structures (ESI Fig. S2†) throughout the optimization of device geometry. The topography of the masters was evaluated by profilometry (Dektak 8 profilometer, with 12.5 μm stylus, operating at 10 mg force, Veeco Metrology Inc.) and the microchannel depth was further measured by optical microscopy.

Poly(dimethylsiloxane), PDMS (Sylgard 184, Dow Corning), was poured over the master, degassed under vacuum, and cured for 1 h at 75 °C in a convection oven. A PDMS slab (typically 5 cm × 2 cm × 4 mm) was cut with a razor blade, carefully pealed off the master, and cored for inputs and outputs. Sharpened stainless steel flat-bore needles (gauge 16 and 19) were used as coring tools. The patterned PDMS surface was cleaned with a brief ethanol rinse and lens tissue, and tape (''Magic'', Scotch) to remove any dust. A microscope glass slide (75 mm × 25 mm × 1 mm, Corning) was cleaned with a 0.5 min exposure to a 60 W oxygen plasma (Anatech-SP100). Both glass and PDMS surfaces were then oxidized for 35 s at 40 W with the oxygen plasma and brought in contact within seconds thereafter, irreversibly sealing the device. An additional heat treatment is known to improve the glass–PDMS seal and returns the microchannels to a hydrophobic native state. The latter can be effectively achieved by annealing the specimen overnight at 120 °C. Finally, the device is connected to syringes (typically 0.5 or 5 mL volume) with Teflon capillary tubing with Luer lock hubs (Hamilton, gauge 20 and 30, according to coring needle), which fits tightly in the cored inlets and outlets.

A typical planar device is depicted in Fig. 4. The main channel (4) is 700 μm wide and 20 mm long, with flow constrictions of 1/3 of the channel's width and 600 μm long; the input channels 1a, b and 2 are 50 μm wide and 3a, b are 400 μm wide; the microchannel height is 100 ± 2 μm throughout.

IV. Instrument operation

IVa. Control and data acquisition

The microfluidic tensiometer is mounted on an inverted optical microscope (Olympus IX71) equipped with an automated XY stage (Prior H107). The Teflon capillaries are nearly filled with input fluids and carefully inserted in the cored inlets to avoid fracturing the PDMS. Typically, 1 mL syringes are used for inputs (1a,b and 2) and 5 mL for focusing inputs 3a,b. Outlet 4 is connected to a 'waste' container with a section of tubing. Computer-controlled syringe pumps (New Era NE-1200/ Braintree BS-8000, or Harvard apparatus PHD-2000) drive the flow inputs. The pumps are connected in series and then, *via* RS-232, onto a desktop computer (2.8 GHz processor and 1 Gb RAM) running LabVIEW 7.0.

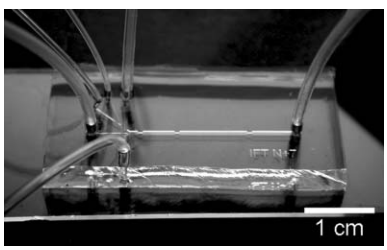

Fig. 4 Microfluidic tensiometer mounted on a microscope glass slide and connected to syringe pumps with capillary tubing.

The device startup procedure is important, as input fluids have different surface preference to channel walls and any trapped air bubbles introduce compressibility and thereby transient flows that may be time-consuming to stabilize. Firstly, air should be excluded by bringing the fluids' menisci near the junction nodes. All inputs should then be ramped up in flow rate, maintaining the meniscus between fluids at the T-junction. Finally, rates 1 and 2 are adjusted to produce drops of adequate dimension and frequency. Drop diameter should be a fraction of the width and height of the constrictions in channel (4) (see discussion in section VI). Typical operating flow rates are $Q(1a + 1b) \approx 15\ \mu L\ h^{-1}$, $Q(2) \approx 15\ \mu L\ h^{-1}$, $Q(3a) = Q(3b) \approx 250\ \mu L\ h^{-1}$. The composition of the suspended drops is set by the ratio of $Q(1a)$ and $Q(1b)$. While we wish to operate the T-junction at relatively low *Ca* number in order to produce controlled plugs (as discussed above), we prefer larger values in this range to increase drop production rates. The resolution of the nominal composition is set by the smallest fluid displacement provided by the pump, a product of the syringe barrel area and stepper motor increment. Small volume syringes (1 mL and below) are used for this purpose and provide 0.35 $\mu L\ h^{-1}$ minimum flow rate (3 nL (motor increment)$^{-1}$).

Fluid drops are imaged with bright-field optical microscopy using 4× or 10× objective lenses (Olympus) having numerical apertures NA = 0.13 and 0.30, respectively. Images are captured with a monochromatic CCD camera (Adimec 1000 M) with 1004 × 1004 pixel resolution, 8-bit depth (256 gray levels) and 50 full frames per second (fps) acquisition rate. The camera is also controlled using LabVIEW, and interfaced to the computer *via* 'Camera Link'. Depending on the objective used, image magnification ranges from (0.74 to 1.85) μm pixel^{-1} and was calibrated using a diffraction grating. Sufficient refractive index mismatch must exist between the fluids in order to obtain satisfactory optical phase contrast between drops and matrix. The microscope light intensity is further adjusted to provide optimal contrast, with the assistance of an image intensity histogram to set the peak gray level intensity to approximately 130. Drops appear dark near the edges. A threshold condition is set to convert the 8-bit image into a binary image that isolates individual drops. A sharp image focusing and accurate thresholding (typically set at 70) contribute to the accuracy of the measurement and will be discussed later.

The image size is adjusted to fit the region of interest (*i.e.*, the entrance or exit of a constriction) and is typically 240 × 1000 pixels. The acquisition of a partial frame allows a higher image acquisition rate of, typically, 100 Hz. This is important in order to obtain a maximum number of images of an

individual drop as it traverses the observation window (typically 5 to 10 or larger, depending on drop velocity). The image integration time must be sufficiently small to generate sharp images of drops, such that their motion during acquisition is less than a full pixel and therefore causes no blurring. Typical integration times range from (30 to 100) μs, depending on drop velocity.

Fig. 2 compiles a series of images that depict the tensiometer operation. The matrix fluid is silicone oil (inputs 2 and 3) and the miscible fluids are water (input 1a) and ethylene glycol (input 1b). Plug formation at the T-junction at low *Ca* number is shown in Fig. 2a. Note the flow of the two miscible streams is laminar because of the low Reynolds number ($Re = \rho uh/\eta$, $O(0.01)$), as seen by their optical contrast. Eventually, diffusion homogenizes the fluids before the plug-to-drop transition occurs. In order to promote mixing, a number of topographic features can be introduced in microchannels.[14–18] The inset in Fig. 2a illustrates a series of asymmetric flow obstacles that induce internal circulation in drops and, thereby, accelerate mixing of its contents. Mixing becomes an important issue when dealing with fluids of higher viscosity or lower compatibility.

IVb. Data analysis and automation

A single LabVIEW program controls the tensiometer and analyzes the data in real-time, using an algorithm outlined below. The program's graphical user interface is depicted in Fig. 5. Our final objective is the computation of eqn (6), which graphically corresponds to a straight line of slope σ. Several unknowns need to be determined for each drop: the undisturbed drop size a_0, the deformation D and its spatial derivative $\partial D/\partial x$, drop velocity u, and extension rate $\dot{\varepsilon} = \mathrm{d}u/\mathrm{d}x$.

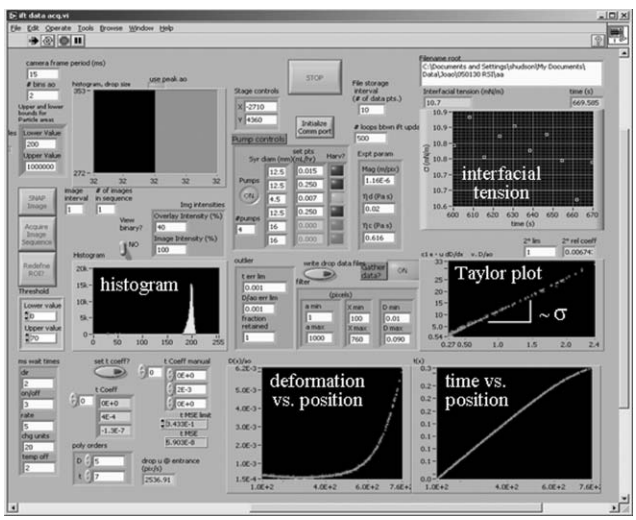

Fig. 5 Flow control and automated image analysis LabVIEW interface panel. The program controls the pump flow rates and device position (with an XY stage), plots the image intensity histogram and sets filters for particle shape analysis (size, position). The images are then analyzed in real time, yielding plots of drop deformation (D) and transit time (t) as a function of position (x). A Taylor plot (see text) and resulting IFT measurements are then calculated at prescribed time intervals.

The viscosities of the fluids (η_d, η_c) are the only input variables in the analysis and should be known accurately, or this uncertainty propagates to σ, according to eqn. (6). For improved accuracy, we compute the Arrhenius temperature dependence of the viscosity from reference data and interpolate η at the relevant temperature, which is recorded during the IFT measurements.

Image analysis proceeds as follows. Since each image may contain more than one drop, an indexing procedure was implemented to identify each drop as it moves through the observation window in a sequence of time frames. The drop production rate should, therefore, be (slightly) slower than the image acquisition rate. If both rates are exactly the same, then drops appear immobile in a time series, and data points cluster at a few positions, which is undesirable.

A single drop is imaged at least several times, at different position x, depending on its velocity. When imaging a constriction entrance, the equilibrium dimensions of a drop a_0 are determined from the first frame when it appears in the field of view and is, therefore, spherical within experimental uncertainty. Sphericity is not prerequisite, however, since a_0 is computed from the volume of the spheroid, according to $a_0 = (ab^2)^{1/3}$. In Fig. 2c, flowing left to right, this corresponds to the first complete drop on the left side. Then, D is computed from the drop's moments of inertia in every frame. The drop's center-of-mass position x is recorded and assigned a time stamp, from which transit time $t(x)$ and velocity u are calculated. Note that the drop velocity is measured directly, instead of computing the entire flow field (by solving the Navier–Stokes equation in a given geometry), which simplifies analysis and improves measurement accuracy.

The procedure is repeated for all drops in each image. The system collects and plots over 100 data points per second. In order to expedite data mining, the images are discarded after being analyzed (image sequences can be saved but the analysis can no longer be carried out in real-time). A histogram of drop dimensions is obtained and only the data belonging to the most populated drop size is analyzed. This data selection filter allows a narrow drop size distribution to be analyzed, if desired, so that the dependence of drop size on interfacial tension or apparent interfacial tension can be tested. (For example, at a given initial surfactant concentration within the drops, the relative amounts of surfactant at the interface depend on drop size, so that if adsorption of surfactant to the interface significantly changes its concentration within the interior, the interfacial tension depends on drop size.) Within a selected size range, D remains proportional to a_0; therefore, we divide D by a_0, before further analysis. The image processing algorithm allows the definition of a spatial region of interest (in pixels) and the selection of a window of relevant drops sizes, which mainly filters out spurious information (*e.g.*, dust). A filter in the deformation data D, defines a minimum (noise) and maximum (for excessive non-spheroidal elongation) criterion for the data to continue to the next stage of analysis.

At prescribed time intervals, compiled data for D/a_o and $t(x)$ are fit to yield the derivatives $\partial D/\partial x$ (remultiplying by a_o) and $\dot{\varepsilon} = \mathrm{d}u/\mathrm{d}x$. Simultaneously, the left hand side term of eqn (6),

$\alpha\eta_c\left(\frac{5}{2\hat{\eta}+3}\dot{\varepsilon}-u\frac{\partial D}{\partial x}\right)$, is fit to a linear function of (D/a_0) to yield slope σ. This value is recorded and updated after another loop of 100–500 data points. When a statistically significant ensemble of σ data is acquired, the input flow rates Q(1a) and Q(1b) are adjusted to change drop composition and the procedure restarts after a transient equilibration time (few minutes).

The tensiometer graphical user interface (Fig. 5) which controls the input flow rates and image thresholding parameters (discussed above), also displays a series of monitoring tools that are updated (with a set periodicity) in real time: (i) a histogram of drop sizes, (ii) drop deformation (normalized to drop size) D/a_0 as function of position x, (iii) drop transit time t as a function of position x, and (iv) a Taylor plot (*viz*. eqn (6)) from whose slope the interfacial tension is obtained. The results obtained for σ are plotted as a function of time in another graph. Any anomaly (*e.g.*, non-linearity of Taylor plot) can be promptly detected and assessed using this ensemble of monitoring tools.

The speed of the IFT measurements is limited by the rate of image acquisition and processing. The image size, acquisition rate and integration time are adjusted in concert to maximize the data collection rate. With the current experimental setup (2.8 GHz processor and 1Gb RAM), our system can analyze images of 240 × 1000 pixels, as fast as the camera acquisition rate of 100 Hz, which translates into a measurement rate superior to 100 data points s^{-1}.

V. Results and discussion

Our microfluidic tensiometry has been validated against conventional pendant drop tensiometry and other measurements reported in the literature with an array of model immiscible systems, involving water, air, silicone and mineral oils, ethylene glycol and glycerol.[1] A rather wide scope of tensions has been measured, ranging from (2.5 to 60) mN m^{-1} so far. In this work, we report in detail a set of measurements on ethylene glycol (EG) in polyphenylmethylsiloxane (PPMS). Further, we investigate a series of binary mixtures of EG and water drops in PDMS oil.

The systems EG/PPMS and EG/water/PDMS were chosen for a number of reasons. Firstly, all are compatible with PDMS devices, which means that soft lithography can be used for microfluidic device fabrication. EG and water are fully miscible liquids, with a low viscosity, and a convenient refractive index contrast, which permits an optical evaluation of mixing in laminar flow and inside drops. PDMS has a suitable optical contrast with both liquids and a rather large variation of σ between EG and water. EG (J.T. Baker, 9300-01), PPMS (Gelest) and PDMS (Gelest) oils have a viscosity of, respectively, 0.02 Pa s, 0.60 Pa s and 1.00 Pa s at 23 °C. Water was obtained from a Millipore ultrafiltration system. Standard uncertainties here are ± one standard deviation, represented in figures by error bars.

Va. Drop dynamics

Fig. 2c shows a typical snapshot of EG drops (≈50 μm radius or 0.5 nL) in PPMS entering a 3:1 channel constriction. Drops accelerate and stretch along the flow direction when entering the contraction. Fig. 6 compiles a data set acquired during a 5 s time interval, corresponding to graphs plotted in real time with the LabVIEW interface (Fig. 5). As described above, drop deformation $D(x)$, transit time $t(x)$, and extension rate $\dot{\varepsilon}(x)$ of

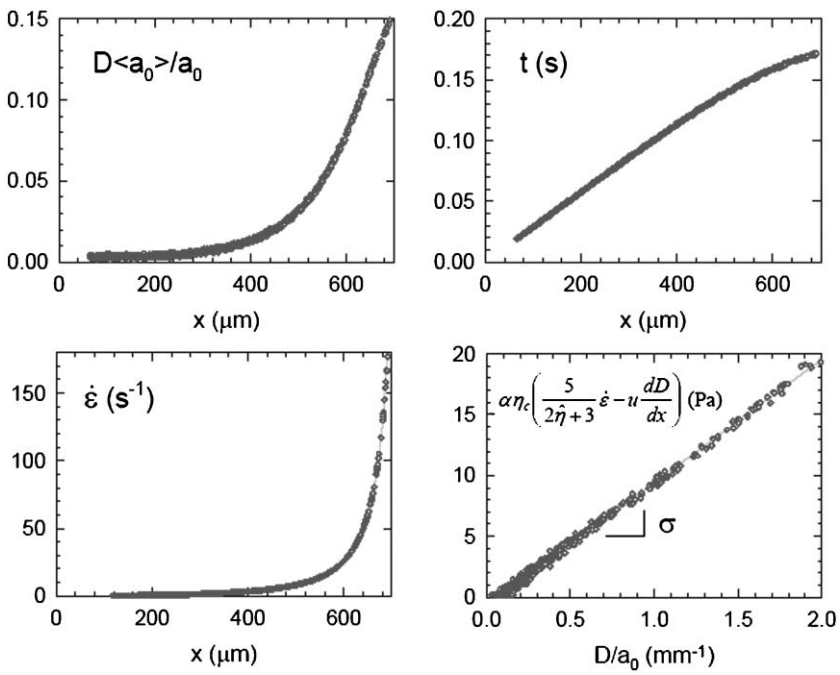

Fig. 6 Typical μIFT data set obtained for ethylene glycol drops (≈40 μm radius) in PPMS oil acquired during a 5 s time interval. Real time particle tracking computes the dimensionless deformation D (normalized by drop size a_0), transit time t (s) along channel and extension rate $\dot{\varepsilon}$ of *all* drops in each image, as a function of channel position. The experimental results are collected during a time interval and then represented in a Taylor plot, whose slope yields the interfacial tension. The dashed lines are fits to the data.

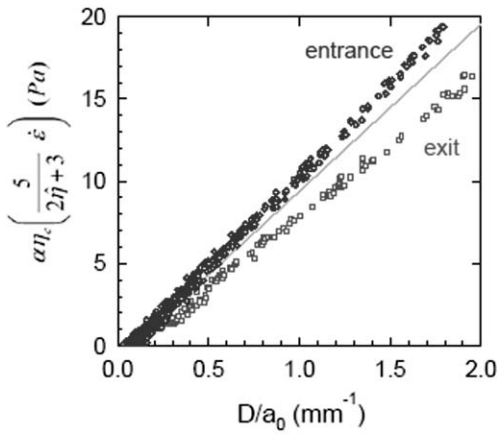

Fig. 7 Quasi-steady-state drop data analysis. Neglecting the second term of the ordinate (Fig. 7b), deviations from steady state become apparent, both at the constriction entrance (○) and exit (□) yielding, respectively, an overestimated or underestimated slope and resulting σ.

the surrounding fluid are plotted against position x along the microchannel. The origin, $x = 0$, is arbitrarily set at the left of the captured image. From each frame, we obtain the position of the center-of-mass and moments of inertia of each drop. $D(x)$ is then computed and divided by the drop size. In Fig. 6, this 'reduced' deformation $D(x)/a_0$ is then multiplied by the average drop size $<a_0>$, to render it dimensionless and normalized. A high order polynomial function (order 4 to 7) fits the data within a region of interest, which excludes high deformations (typically above 0.10) and drops inside the contraction (where the deformation begins to relax). The transit time $t(x)$ is a measure of drop velocity and shows continuous acceleration upon approaching the flow contraction. The extension rate $\dot{\varepsilon}(x)$ is then computed from $t(x)$ measurements. Finally, a Taylor plot is obtained from the direct observables and their derivatives, as shown in the last panel. The data points are denser (and noisier) at low deformations (D/a_0), corresponding to most of the drop's travel path and become sparser at higher deformations, since the contraction is sudden and drops only briefly experience high D. The interfacial tension is obtained directly from the slope of the Taylor plot, which is linearly fit over a statistically significant interval of D/a_0 (here [0.3, 2]).

The ordinate of the Taylor plot comprises two terms, shown in eqn (6). The first gives the steady state deformation and is governed by $\dot{\varepsilon}$ at that location x. The second term captures the drop dynamics history, which may be out of equilibrium. Fig. 7 demonstrates graphically the importance of both terms in our measurements. The solid line is the full calculation, corresponding to the Taylor plot of Fig. 6. Deviations from steady state are apparent, when only the first term is calculated, showing a positive deviation of the slope (and an apparent higher σ) when drops flow toward the contraction (○, 'entrance'). An assumption of quasi-steady state (neglect second term) is therefore inappropriate. In other words, the instantaneous deformation of the drop lags the steady state deformation.

The measurement and analysis shown hitherto concern fluid drops entering a flow constriction. The tensiometer can also analyze drops exiting flow constrictions. In this case, however, the determination of drop dimensions from its first appearance in the field of view becomes less accurate because of its initial deformation (*viz*. Fig. 2b). The steady state approximation remains invalid for exiting drops, and Taylor plots now show *negative* deviations of the slope (□ 'exit'), as shown in Fig. 7. As expected, both 'entrance' and 'exit' measurements overlap on the solid line when the full Taylor analysis is carried out (data points not shown for clarity).

Vb. Binary mixtures

We now consider measurements of interfacial tension of binary mixtures. As discussed above, we choose EG + water in PDMS oil for this demonstration and use a single device with two miscible inputs. The σ of the pure liquids and six intermediate compositions were measured (Fig. 8). The solid line is a guide to the eye mixing rule computed as the geometric average of the pure components IFT as $1/\sigma\ (\phi) = \phi/\sigma_{EG} + (1 - \phi)/\sigma_{water}$, where ϕ is the volume fraction of EG. A linear rule of mixtures is never expected, because the interface will accumulate some degree of the component that reduces its tension. The degree of accumulation depends of course on the molecular interactions, so that mixtures having a smaller free energy of mixing accumulate more, and the mixing rule may be highly non-linear, with derivative $d\sigma/d\phi$ increasing near the component with largest pure interfacial tension.[26] A detailed discussion of the IFT of mixtures lies outside the scope of this paper.

In the context of mixing miscible fluids, flow stability is most important. Capacitance in inputs 1a or 1b (Fig. 1) gives rise to unsteady flow in channel 1 and very irregular fluid composition, when the viscosity of the fluid depends on its composition. For example, the viscosity of mixtures of water and ethylene glycol depend on composition and range between limits that differ by approximately a factor of 20. Consider capacitance in the source that contains water (*e.g.*, 1a). A fluctuation that increases the concentration of ethylene glycol (1b) in channel 1 increases the viscosity and reduces the flow rate, particularly in channel 1a, augmenting the fluctuation and "charging" the capacitor. When the capacitor (C_{1a}) is charged sufficiently, the flow of water into channel 1 finally increases, decreasing the viscosity there, triggering a further increase in flow rate of the water, discharging the capacitor.

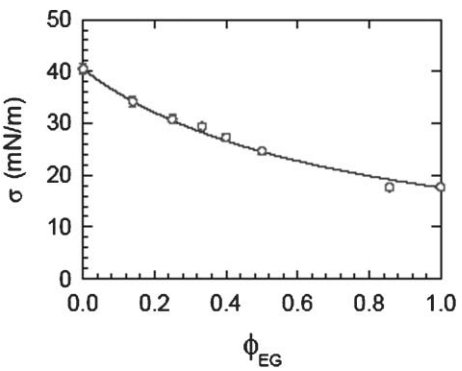

Fig. 8 Interfacial tension of water/ethylene glycol mixtures (binary drops) in PDMS oil, as a function of composition. The solid line is a guide to the eye, given by the geometric average of the pure liquids' σ.

The system cycles in this way. These oscillations differ from those transients in mean flow rate that decay over time (*e.g.*, after a commanded change in flow rate, see section IIIa). Fortunately, in our experiments, even small amplitude cycles are evident from any motion of the diffuse contact line between water and ethylene glycol streams (see the blurry dark line at the Y-junction at the top of Fig. 2a). When composition fluctuations (and accompanying flow rate variations) occur, this line oscillates laterally. Such enduring fluctuations occur when air is in the system, or when using deformable plastic syringes or flexible tubing, whose flexibility sets the value of the capacitors C_{1a} and C_{1b}, and the amplitude of flow rate oscillations. Glass syringes with rigid metal plungers and rigid tubing reduce this amplitude to negligible values. The scenario is relatively much more stable, when the two miscible fluids possess nearly the same viscosity, such as when mixing water and a dilute solution of surfactant.

Vc. Factors affecting measurement precision and accuracy

We have examined in detail the fabrication and operation of the microfluidic tensiometer and demonstrated the measurement of a binary liquid mixture. Here, we elaborate certain factors that contribute appreciably to the precision and accuracy of the σ measurements. Specifically, we consider the influence of focusing and threshold level in the image analysis, the effect of finite-sized channels, and flow rate.

The drop shape analysis is carried out on binary images obtained by thresholding monochromatic 8-bit images. The adjustment of the image light intensity and focusing, and the setting of a binary threshold is currently done manually. The LabVIEW interface displays an intensity histogram and provides the option of partially overlaying the binary image over its gray scale source, which makes the process rather straightforward.

A well-focused drop exhibits a fine dark edge that, if the image is thresholded adequately, accurately identifies drop shape. Poor focusing leads to the appearance of either a dark or a light halo surrounding a drop, depending on whether the drop position is above or below the focusing plane. A dark halo can be particularly detrimental as, at a constant threshold level, the drop appears larger in all directions (but not proportionally) and therefore exhibits a higher apparent interfacial tension. In extremely unfocused images (approaching the objective's focal depth), offsets in σ of up to 20% were observed. Conversely, a light halo is not so damaging, as the thresholded drop size (inside the dark boundary) is nearly unchanged.

An accurately set image threshold value is also necessary for accurate σ measurements, although its setting is more lenient; even the most inadequate setting leads to errors of at most 5%. On a focused image, a low threshold eventually reduces the drop size and results in lower apparent tensions; the opposite occurs for high thresholds. An important difference with the effect of image focusing is that a poor threshold setting eventually results in irregular drop contours due to image noise. If the threshold value is appropriate, the contour is always smooth, even when focusing is poor.

Drop confinement in a microfluidic environment was a matter of concern throughout the development of this tensiometry approach. Lubrication forces are expected to become relevant when the continuous matrix fluid becomes confined either by microchannel walls or between multiple subsequent drops. For example, these forces can cause the drop to relax more slowly[27] and move slower than the surrounding fluid and relative to its local surroundings.[28] These effects are most significant when $\hat{\eta}$ is large. Moreover, interaction between adjacent drops is negligible if the distance between their centers is slightly larger than the distance between confining walls.[29] To test the effect of channel walls, we systematically increased the drop size until the diameter became comparable to the channel's smallest dimension, usually its height. For systems having small $\hat{\eta}$ (*e.g.*, 0.03), we found that the measurement of σ remained unchanged when the drop diameter is adjusted between 0.2 h and 0.7 h and was not affected until the drop diameter was nearly 0.8 h (Fig. 9). More significant effects are likely for larger $\hat{\eta}$, since the drop then experiences a significant drag force,[28] as noted above.

Finally, the flow rate (of drops and surrounding matrix fluid) is not expected to affect the determination of σ of homogenous droplets. In the presence of interfacially active components (*e.g.*, surfactants), however, flow rate or drop velocity is expected to influence interfacial dynamics and will be discussed separately.

VI. Conclusions

We have proposed a novel approach to interfacial tensiometry based on a dynamic analysis of the shape of drops prepared and interrogated in microfluidics. In this paper, we describe in detail the design and fabrication of such microfluidic devices and examine the image and data analysis algorithm that measure interfacial tension σ directly. We investigate the effect of bounded flow when drops are sufficiently large. Moreover, for the first time, we also implement the microfluidic tensiometer in the study of mixtures, by producing and testing suspended fluid drops of prescribed composition.

Microfluidic tensiometry offers considerable advantages compared to traditional measurement of σ. First, it is

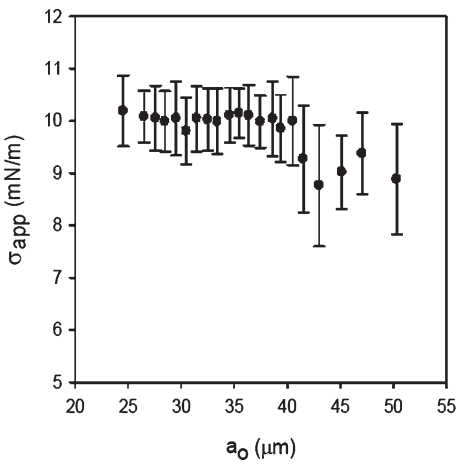

Fig. 9 Apparent interfacial tension of ethylene glycol drops (0.02 Pa s) suspended in PPMS500 (0.60 Pa s), as a function of drop radius at 23 °C. The minimum channel dimension is the height $h = 100 \pm 2$ μm.

intrinsically a fast measurement technique since microdrops can be produced and interrogated rapidly in microfluidics. We have demonstrated that image acquisition and automated drop shape analysis could equally be carried out at a fast rate. These premises combined enable an acquisition rate of $\approx$100 data points s^{-1}, and effectively σ measurements in approximately 1 s. Further, our approach utilizes 'passive' flow control, which means that drops are simply convected through a microchannel whose shape induces the desired flow field (an extensional flow gradient) for testing. In previous work, we have shown that a microfluidic 4-roll mill[13] could 'actively' (by adjusting flow rates around a cross-channel geometry) generate an array of tunable flow types, including pure extension. However, passive flows such as those exploited in the present tensiometer, are rather more efficient and amenable to high throughput measurements of fluids. Microfluidics, generally, utilizes very small amounts of reagents (in our case, in the order of micro to milliliters), which can be valuable for applications involving scarce or expensive supplies (*e.g.*, custom-synthesized tensioactive materials). The device fabrication and operation is itself rather inexpensive and relatively simple. Microchannels provide a unique environment for the production of controlled multiphase flows which, in the present case is a string of regularly spaced monodisperse drops. Despite the operation at low Reynolds numbers and prevalence of laminar flows, a number of simple strategies enable the mixing of fluid components in continuous miscible or immiscible flows. In the tensiometer shown here, we have prepared two-component drops for demonstration purposes, but additional miscible inputs may be readily included.

Interfacial microfluidic tensiometry is relevant for at least two scientific areas of both fundamental and technological interest. The first has already been mentioned and concerns complex mixtures and formulations, which can be prepared and studied *in-situ* with unprecedented measurement speed, utilizing minimal reagent volumes. The second concerns interfacial dynamics and aging and was not discussed in this paper. Microfluidics is remarkably well suited for studying reaction kinetics as the relationship between time and space emerges naturally as fluids convect along microchannels. A number of applications in chemical and biological analysis implemented in microfluidics have already benefited from this attractive distance-to-time transformation.[17,18] We will report separately on the use of microfluidic tensiometry to study interfacial dynamics in surfactant containing emulsions.

Acknowledgements

The authors thank Kathryn L. Beers, Jack F. Douglas, Eric J. Amis, Hua Hu and Frederick Phelan Jr for useful discussions and support throughout this project. Support from the NIST Materials Science Engineering Laboratory Director's Reserve and the NIST Combinatorial Methods Center and members ICI/National Starch and Procter & Gamble is greatly appreciated.

References

1 S. D. Hudson, J. T. Cabral, W. J. Goodrum, Jr, K. L. Beers and E. J. Amis, *Appl. Phys. Lett.*, 2005, **87**, 081905.
2 A. I. Rusanov and V. A. Prokhorov, Interfacial Tensiometry in *Studies in Interface Science, Vol. 3*, ed. D. Möbius and R. Miller, Elsevier, Amsterdam, 1996.
3 Drops and Bubbles in Interfacial Research in *Studies in Interface Science, Vol. 6,*, ed. D. Möbius and R. Miller, Elsevier, Amsterdam, 1998.
4 J. Drelich, Ch. Fang and C. L. White, Measurement of Interfacial Tension in Fluid–Fluid Systems in *Encyclopedia of Surface and Colloid Science*, Marcel Dekker, New York, 2002, p. 3152.
5 S. S. Dukhin, G. Kretzschmar and R. Miller, Dynamics of Adsorption at Liquid Interfaces: Theory, Experiment, Application, in *Studies in Interface Science*, ed. D. Möbius and R. Miller, Elsevier, Amsterdam, 1995, vol. 1.
6 C. A. MacLeod and C. J. Radke, *J. Colloid Interface Sci.*, 1993, **160**, 435.
7 T. F. Svitova, M. J. Wetherbee and C. J. Radke, *J. Colloid Interface Sci.*, 2003, **261**, 170.
8 T. Thorsen, R. W. Roberts, F. H. Arnold and S. R. Quake, *Phys. Rev. Lett.*, 2001, **86**, 4163.
9 S. L. Anna, N. Bontoux and H. A. Stone, *Appl. Phys. Lett.*, 2003, **82**, 364.
10 D. R. Link, S. L. Anna, D. A. Weitz and H. A. Stone, *Phys. Rev. Lett.*, 2004, **92**, 054503.
11 P. Garstecki, H. A. Stone and G. M. Whitesides, *Phys. Rev. Lett.*, 2005, **94**, 164501.
12 A. S. Utada, E. Lorenceau, D. R. Link, P. D. Kaplan, H. A. Stone and D. A. Weitz, *Science*, 2005, **308**, 537.
13 S. D. Hudson, F. R. Phelan, Jr., M. D. Handler, J. T. Cabral, K. B. Migler and E. J. Amis, *Appl. Phys. Lett.*, 2004, **85**, 336.
14 A. D. Stroock, S. K. W. Dertinger, A. Ajdari, I. Mezic, H. A. Stone and G. M. Whitesides, *Science*, 2002, **295**, 647.
15 R. H. Liu, M. A. Stremler, K. V. Sharp, M. G. Olsen, J. G. Santiago, R. J. Adrian, H. Aref and D. J. Beebe, *J. Microelectromech. Syst.*, 2000, **9**, 190.
16 T. J. Johnson, D. Ross and L. E. Locascio, *Anal. Chem.*, 2002, **74**, 45.
17 H. Song, J. D. Tice and R. F. Ismagilov, *Angew. Chem., Int. Ed.*, 2003, **42**, 768.
18 J. D. Tice, H. Song, A. D. Lyon and R. F. Ismagilov, *Langmuir*, 2003, **19**, 9127.
19 Reviews on microfluidics and applications: G. M. Whitesides and A. D. Stroock, *Phys. Today*, 2001, **54**, 42; P. Mitchell, *Nat. Biotechnol.*, 2001, **19**, 717; J. W. Hong and S. R. Quake, *Nat. Biotechnol.*, 2003, **21**, 1179; R. F. Ismagilov, *Angew. Chem., Int. Ed.*, 2003, **42**, 4130; H. A. Stone, A. D. Stroock and A. Ajdari, *Annu. Rev. Fluid Mech.*, 2004, **36**, 381.
20 G. I. Taylor, *Proc. R. Soc. London, Ser. A*, 1932, **138**, 41; G. I. Taylor, *Proc. R. Soc. London, Ser. A*, 1934, **146**, 501.
21 J. M. Rallison, *Annu. Rev. Fluid Mech.*, 1984, **16**, 45.
22 H. Yamane, M. Takahashi, R. Hayashi, K. Okamoto, H. Kashihara and T. Masuda, *J. Rheol.*, 1998, **42**, 567.
23 Certain commercial materials and equipment are identified in this paper in order to adequately specify the experimental procedure. In no case does such identification imply recommendation or endorsement by the National Institute of Standards and Technology, nor does it imply that these are necessarily the best available for the purpose.
24 J. T. Cabral, S. D. Hudson, C. Harrison and J. F. Douglas, *Langmuir*, 2004, **20**, 10020.
25 C. Harrison, J. T. Cabral, C. Stafford, A. Karim and E. J. Amis, *J. Microeng. Micromech.*, 2004, **14**, 153.
26 The properties of gases and liquids, R. C. Reid, J. M. Prausnitz and B. E. Polling, McGraw-Hill, New York, 1987.
27 T. Mikami and S. G. Mason, *Can. J. Chem. Eng.*, 1975, **53**, 372.
28 G. Hetsronni, S. Haber and E. Wacholder, *J. Fluid Mech.*, 1970, **41**, 689.
29 B. P. Ho and L. G. Leal, *J. Fluid Mech.*, 1975, **71**, 361.
30 D. C. Duffy, J. C. McDonald, O. J. A. Schueller and G. M. Whitesides, *Anal. Chem.*, 1998, **70**, 4974.

